Progress in Physics of Applied Materials 7 (2027), Serial Number 14, 47-61

Semnan University

Progress in Physics of Applied Materials

journal homepage: https://ppam.semnan.ac.ir/

An Investigation on the Corrosion and Electrical Behavior of Co-coated Crofer 22 APU Bipolar Plates for PEMFCs

Farhad Mohsenifar [a,b], Hadi Ebrahimifar [c*], Ahmad Irannejad [b]

[a] *Mechanical Engineering Department, Higher Education Complex of Bam, Bam, 76615-314, Iran*

[b] *Department of Materials Engineering and Metallurgy, Shahid Bahonar University of Kerman, Kerman, 76169-133, Iran*

[c] *Department of Materials Engineering, Faculty of Mechanical and Materials Engineering, Graduate University of Advanced Technology, Kerman, 76315-117, Iran*

ARTICLE INFO

Article history:
Received: 23 May 2026
Revised:8 July 2026
Accepted: 14 July 2026
Published online: 2 August 2026

Keywords:
Electrodeposition;
Bipolar plates;
Corrosion;
Interfacial contact resistance.

ABSTRACT

In this study, a cobalt coating was deposited onto stainless steel bipolar plates used in proton exchange membrane fuel cells (PEMFCs) via the direct current electrodeposition technique. The coating's surface morphology and phase composition were assessed using field emission scanning electron microscopy (FESEM) coupled with energy-dispersive spectroscopy (EDS) and X-ray diffraction (XRD), respectively. The corrosion behaviour of both coated and uncoated samples was evaluated by potentiodynamic polarization and electrochemical impedance spectroscopy (EIS) in simulated cathodic and anodic environments of the PEMFC. The chemical states of the samples' surface before and after corrosion were analyzed using X-ray photoelectron spectroscopy (XPS). To assess changes in electrical performance, the interfacial contact resistance (ICR) of each sample was determined before and after corrosion. The potentiodynamic polarization results demonstrated that the application of the cobalt coating on the steel substrate led to a reduction in the corrosion current density by approximately 31 and 25 times in the simulated cathodic and anodic environments, respectively. XPS analysis confirmed the formation of cobalt oxide on the coated steel surface after corrosion, while the corrosion layer on the bare steel consisted of iron and chromium sulfides and hydroxides. The results revealed that under a clamping force of 1.4 MPa, the coated specimen exhibited a lower ICR (2.42 mΩ cm^2) compared to the bare sample (30.49 mΩ cm^2). Moreover, an increase in ICR values was observed for both specimens after the potentiodynamic polarization test.

1. Introduction

Renewable energy generation via electrochemical systems like PEMFCs is a promising approach to address fossil fuel depletion and environmental issues. PEMFCs offer key advantages including low-temperature operation (~70°C), a wide power output range (1W-500kW), and portability [1-3].

A single PEMFC unit, consisting of an anode, cathode, and polymer membrane, typically produces a voltage of 0.5-0.7 V. To achieve higher efficiency, individual cells are connected through conductive bipolar plates [4,5]. These plates significantly influence the overall weight, cost, and mechanical strength of the fuel cell stack, often more so than other components [6-10]. Graphite, carbon–polymer composites, and metals are the three common categories of materials used for bipolar plates [11-14]. Among these, metallic bipolar plates offer superior mechanical strength, high thermal and electrical conductivity, lower production costs, and easier fabrication [15]. However, their susceptibility to corrosion remains a major drawback. The release of metal ions during corrosion can poison the

* Corresponding authors.
E-mail addresses: H.ebrahimifar@kgut.ac.ir

Cite this article as:

Mohsenifar F., Ebrahimifar H., and Irannejad A., 2026. An Investigation on the Corrosion and Electrical Behavior of Co-coated Crofer 22 APU Bipolar Plates for PEMFCs. *Progress in Physics of Applied Materials*, *7*(1), pp.47-61.DOI: 10.22075/ppam.2026.40824.1213

polymer membrane and deteriorate cell performance [16,17]. In addition, the formation of surface oxide films on metallic plates, particularly stainless-steel ones, increases interfacial contact resistance and adversely affects electrical conductivity [18,19]. Although stainless steels exhibit adequate corrosion resistance in corrosive environments, the acidic conditions, and moderate temperatures (~70 °C) of PEMFC operation can degrade the passive film on the steel surface, leading to accelerated corrosion [20,21]. In fact, fluoride ions released via membrane degradation induce the corrosion of steel bipolar plates. Furthermore, the dissolution of these metallic plates leads to the liberation of metal cations, which subsequently contaminates the fuel cell membrane. An additional constraint of steel bipolar plates involves the rise in ICR resulting from the development of passive layers on their surface [22,23]. To address these limitations, various protective coatings such as nitrides, carbides, metal oxides, carbon-based films, transition metals, noble metals, and conductive polymers have been proposed to improve the corrosion resistance of stainless-steel bipolar plates [24]. However, transition metal coatings have emerged as superior alternatives due to their exceptional electrochemical stability and enhanced electrical conductivity. The improved durability of steel plates coated with transition metals is largely attributed to the formation of stable and adherent metallic oxide layers on the steel surface [25,26].

Several deposition techniques, including electroplating [27], magnetron sputtering [28], pack cementation [29], ion implantation [30], chemical vapor deposition (CVD) [31], physical vapor deposition (PVD) [32], and electroless deposition [33] have been employed to produce such coatings.

Both mono-metallic and multi-metallic electroplated coatings of transition metal have exhibited significant efficacy for use in steel bipolar plate applications. Chiang et al. [34] demonstrated that an electroplated nickel layer significantly enhanced the corrosion resistance of carbon steel. This behaviour can be ascribed to the nickel coating's ability to suppress iron oxide formation on the steel substrate under fuel cell operating conditions. Rashtchi et al. [35] found that Ni-Mo coating reduced both the corrosion current density and ICR of 316L stainless steel. They found the Ni-Mo coating exhibiting a corrosion potential within the stainless steel's passive region, which effectively mitigated the risk of localized corrosion occurrence.

The utilization of transition metals such as Cr, W, Ta, Nb for the surface modification of steel bipolar plates, employing techniques such as plasma, has also been extensively studied [36-39]. Li et al. [36] demonstrated that in simulated PEMFC cathodic environment, the corrosion current density of uncoated 316L stainless steel bipolar plates was 63 μA cm^{-2}, whereas this value decreased to 13 μA cm^{-2} in the presence of a tantalum coating.

Recently, bimetallic, as well as, multilayer coatings composed of transition metals have been utilized to improve the performance of steel bipolar plates [40-43]. Gago et al. [43] demonstrated that ICR value of Au/Ti-coated bipolar plate reduced to 8.6 mΩ cm^2 at a clamping force of 1.4 MPa, which has been attributed to the enhancement of surface roughness provided by the coating.

To the best of the authors' knowledge, the influence of pure cobalt coatings on the performance of steel bipolar plates has not yet been investigated. Furthermore, the application of metallic cobalt coatings via electrodeposition enables the maintenance of the surface electrical properties at a satisfactory level. Additionally, it is expected that the formation of cobalt oxides on the steel bipolar plates surface in the corrosive environment will provide a protective barrier [44].

2. Experimental

2.1. Coating Preparation

In this work, ferritic stainless steel Crofer 22 APU, containing 22.7 wt% Cr, 0.38 wt% Mn, 0.02 wt% Si, 0.01 wt% C, 0.02 wt% Ni, 0.02 wt% Al, 0.07 wt% Ti, 0.06 wt% La, and the balance Fe, was chosen as the substrate material for PEMFC bipolar plates. For cobalt (Co) electrodeposition, steel cathodes (10 mm × 10 mm × 2 mm) and a platinum-coated titanium anode (20 mm × 20 mm) were employed in the electroplating setup. Prior to coating, the steel samples underwent a multistep surface preparation procedure consisting of:

(1) mechanical grinding with SiC abrasive papers of 400, 800, 1200, 1500, 2000, and 2500 grit sizes;

(2) ultrasonic cleaning in acetone to remove contaminants;

(3) electropolishing in phosphoric acid at a current density of 500 mA cm^{-2} for 2 min; and

(4) surface activation in a mixed acid solution containing 5 wt% HNO_3 and 25 wt% HCl for 1 min. The composition of the electroplating bath and the deposition parameters are summarized in Table 1.

Table 1. The composition and conditions of the electrolyte used for the electrodeposition of cobalt coating.

Materials and conditions	details
Cobalt sulphate, heptahydrate ($CoSO_4.7H_2O$)	28.11 g L^{-1} (0.1 M)
Boric acid (H_3BO_3)	61.84 g L^{-1} (1 M)
Ammonium sulphate $(NH_4)_2SO_4$	13.2 g L^{-1} (0.1 M)
Current density	150 mA cm^{-2}
Temperature	25 ºC
pH	2
Time	45 min

2.2. Surface Characterizations

The surface morphology of the samples before and after corrosion, as well as the cross-sectional analysis of the coated sample, was examined using a field emission scanning electron microscope (FESEM, model MIRA3 TESCAN-XMU) equipped with EDS. Phase analysis of the coating was performed using XRD with a Philips X'Pert High Score diffractometer employing Cu Kα radiation (λ =

1.5405 Å). The identification of phases and their associated characteristic peaks was carried out via Xpert Highscore Xpert 3.05 software. The chemical state of the coating surface before and after corrosion was investigated by XPS using a SPECS instrument; specifically, as-coated sample was cleaned using argon sputtering prior to XPS characterization, whereas post-corrosion analysis was performed immediately on the as-received samples.

2.3. Electrochemical Measurements

For corrosion testing, an electrochemical cell was configured using a saturated calomel electrode (SCE) as the reference electrode, a platinum electrode as the counter electrode, and the test specimen - either uncoated or coated - as the working electrode. The corrosive medium for all experiments was a 0.5 M H_2SO_4 solution containing 2 ppm HF, maintained at 70 °C. To better replicate the operational conditions of a PEMFC, the simulated anodic and cathodic environments were made by purging hydrogen and air into the electrolyte, respectively. Prior to testing, the samples were placed in the corrosive solution for 1 h to ensure stable electrochemical condition.

Potentiodynamic and potentiostatic polarization measurements were conducted using a Metrohm Autolab PGSTAT302N potentiostat/galvanostat system. Potentiodynamic polarization curves were generated by sweeping the potential at a rate of 1 mV s^{-1}, and the resulting data were analyzed using CorrView 3.3b software.

During potentiostatic testing, the temporal variation of current was recorded at -0.1 V and +0.6 V for the simulated anodic and cathodic conditions, respectively.

EIS measurements were performed at the open-circuit potential with a Wonatech ZIVE SP1 system over the frequency range of 0.01 Hz to 100 kHz, and the impedance spectra were fitted using ZView 3.1 software.

2.4. ICRs Measurements

Two experimental configurations were employed [45]: in the first (Figure 1a), a gas diffusion layer (GDL) was placed between two copper current collector plates; in the second (Figure 1b), two GDLs were positioned between the copper plates, with the tested sample inserted between them. A compressive load ranging from 0.3 MPa to 5 MPa was applied using a hydraulic system. Under each pressure, a current of 0.1 A was imposed, and the corresponding voltage drop was measured to calculate the electrical resistance according to Ohm's law (Eq. 1).

$$R = \frac{VA_S}{I} \quad (1)$$

In this equation, R denotes the resistance, V is the voltage drop, I is the applied current, and A_s denotes the surface area of the sample.

The resistance values obtained from the setups shown in Figures 1a and 1b are represented as R1 and R2, respectively, and are calculated using Eq. 2 and Eq.3.

$$R_1 = 2R_{Cu} + 2R_{Cu/GDL} + 2R_{GDL} \quad (2)$$

$$R_2 = 2R_{Cu} + 2R_{Cu/GDL} + 2R_{GDL} + 2R_{Bp/GDL} + 2R_{Bp} \quad (3)$$

Since the intrinsic resistance of the BP is negligible, the ICR at the interface between the BP and the GDL was determined based on Eq. 4.

$$R_{Bp/GDL} = \frac{R_2 - R_1}{2} \quad (4)$$

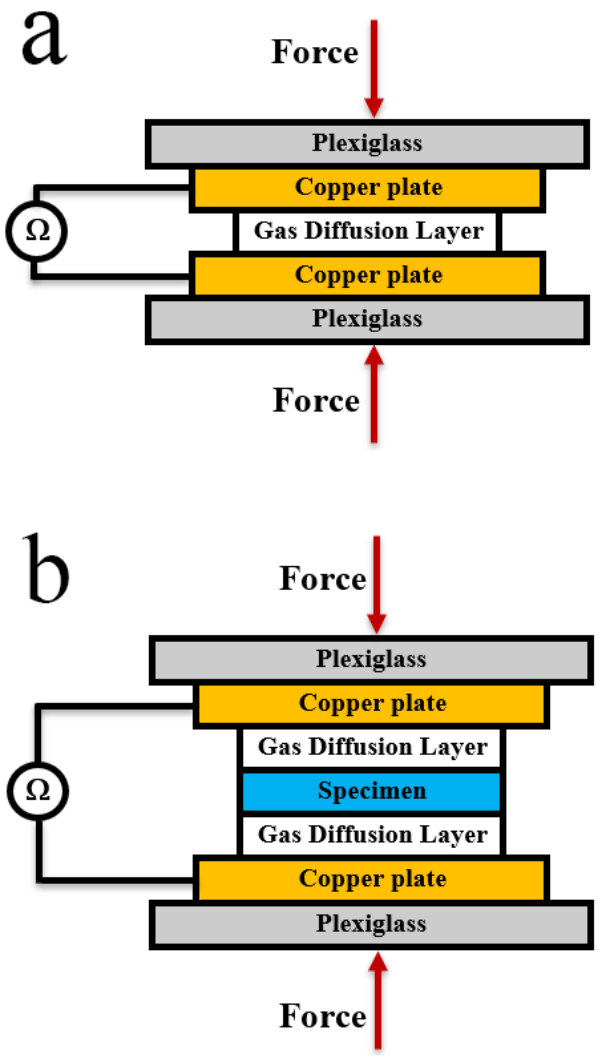

Fig. 1. A schematic of ICR measurement setup (a) without specimen and (b) with specimen.

3. Results and Discussion

3.1. Microstructure of Coating

Figs. 2a and 2b display the surface morphology of the cobalt coating applied on the substrate at different magnifications. The coating exhibits a cauliflower-like structure composed of grains approximately 20 µm in size. The elemental mapping analysis (Figure 2c) shows a very low content of substrate elements (Fe and C), confirming the high density and continuity of the deposit. Furthermore, the EDS elemental map (Figure 2d) demonstrates a uniform spatial distribution of cobalt across the coating.

The XRD pattern of the coated specimen (Figure 3) reveals diffraction peaks at 2θ = 41.68°, 44.8°, 47.56°, 75.96°, 84.2°, 90.64°, 92.56°, 94.72°, and 98.72°, which correspond to the (100), (002), (101), (110), (103), (200), (112), (201), and (104) planes of hexagonal cobalt (JCPDS Card No. 05-0727). The formation of hexagonal cobalt rather than its fcc phase is attributed to the pH of the electrolyte (pH = 4.5) used during electroplating [46]. Substrate-related peaks corresponding to Fe (JCPDS Card No. 00-001-1262) were also observed at 2θ = 44.8° and 82.36°.

The high-resolution XPS spectrum of the electrodeposited cobalt layer (Figure 4) exhibits binding energy peaks at 778.16 eV (Co 2p3/2) and 793.09 eV (Co 2p1/2), characteristic of metallic cobalt, which are consistent with the values reported by Kerrigan [47]. The absence of cobalt oxide peaks is attributed to the surface sputtering conducted prior to analysis. Cross-sectional imaging of the coating and its line-scan profile (Figures 5a and 5b) reveal a dense cobalt-rich layer approximately 15 μm thick.

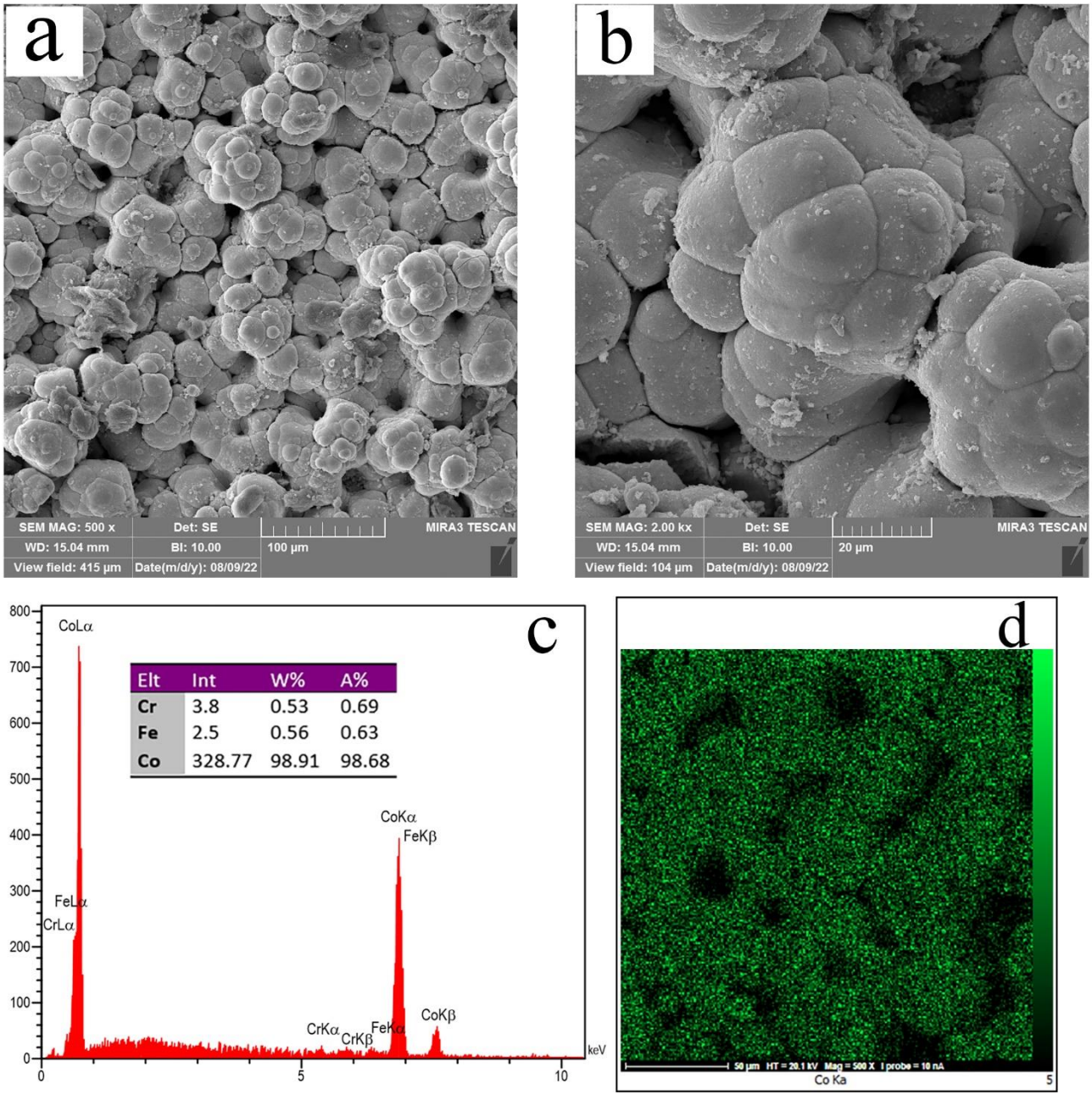

Fig. 2. (a and b) FESEM micrographs at different magnifications, (c) EDS analysis and (d) EDS mapping of the Co-coated steel.

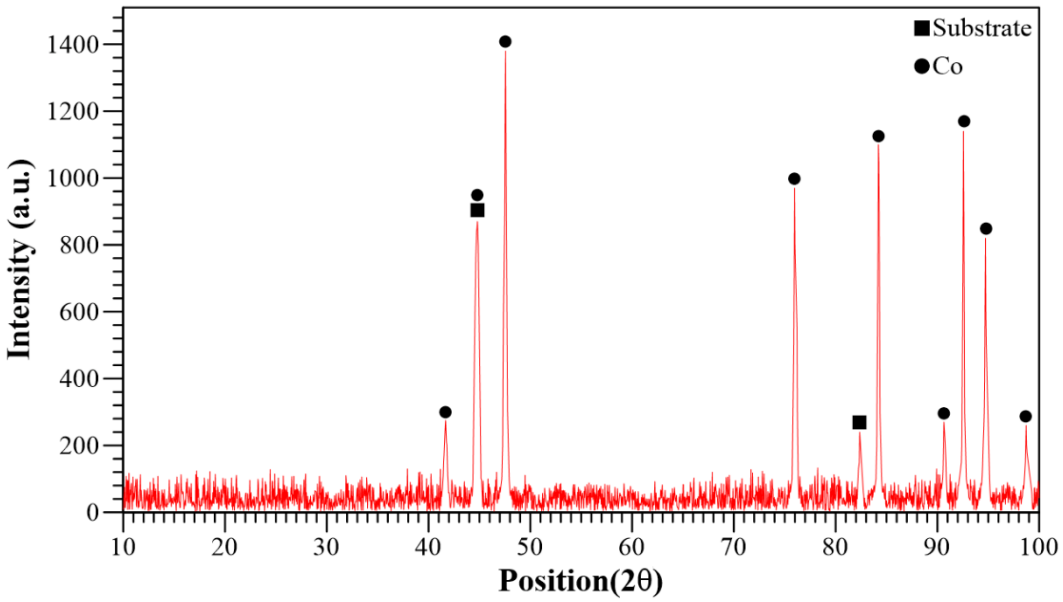

Fig. 3. X-ray diffraction pattern of the cobalt coating electrodeposited on Crofer 22 APU bipolar plate.

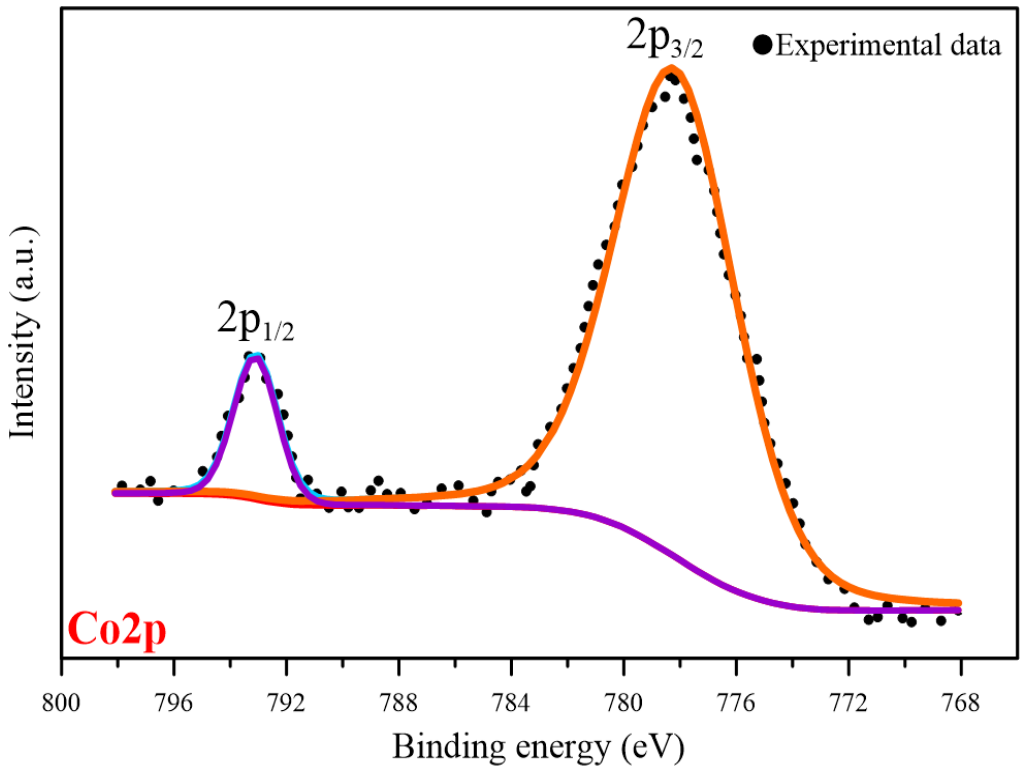

Fig. 4. High-resolution spectra and fitted curve of the cobalt coating electrodeposited on Crofer 22 APU bipolar plate.

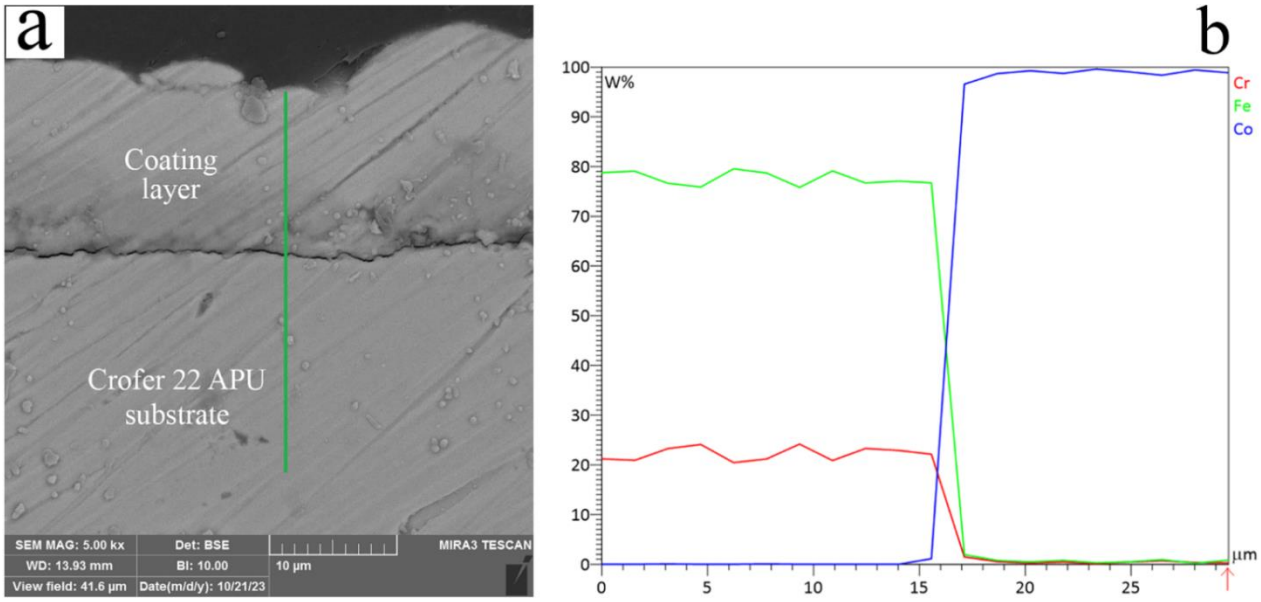

Fig. 5. (a) FESEM cross-section micrograph and (b) EDS line scan of Co-coated Crofer 22 APU steel.

3.2. Electrochemical Analysis

3.2.1. Open Circuit Potential

The open-circuit potential (OCP) variations of the samples during one hour of immersion in simulated anodic and cathodic environments at 70 °C are depicted in Figures 6a and 6b, respectively. For the uncoated specimen, the potential in both environments initially increased sharply toward more noble values, reaching peaks at around 900 s and 650 s in the cathodic and anodic media, respectively, before gradually declining to a steady-state potential. This transient behavior, characterized by an initial rapid rise followed by a gradual decline, is attributed to the formation and subsequent partial breakdown of passive oxide films on the surface [48].

The coated samples display a similar initial increase before reaching stable and nearly constant potentials. This trend can be attributed to the formation of a passive film on the coating surface during the initial stages of exposure (as reflected by the potential increase) and then, the stability of the formed passive film, which leads to potential stabilization [49]. The steady-state OCPs for the uncoated specimen are -0.05 V (cathodic) and -0.01 V (anodic), whereas those for the coated sample are -0.03 V and 0.05 V, respectively. The more active potential observed for the uncoated sample in both environments indicates its higher susceptibility to corrosion under the simulated fuel cell conditions [50].

3.2.2. Potentiodynamic Polarization

The potentiodynamic polarization curves of the samples tested in cathodic and anodic environments at 70 °C, are illustrated in Figures 7a and 7b, respectively, and the associated electrochemical parameters are summarized in Table 2. The polarization resistance values were estimated using the Stern-Geary equation. Tafel extrapolation of the potentiodynamic polarization curves was carried out in triplicate via CorrView 3.3b software. The results in Table 2 are reported as the mean value ± standard deviation of these data.

As observed in Figure 7, Tafel curve of the uncoated sample exhibits three distinct regions: active, passive, and trans-passive. The presence of the trans-passive region signifies the instability of the passive film formed on the sample surface. In the Tafel curves of the coated samples, the active-passive transition is not observed; however, the anodic Tafel slope (β_a) for these samples is greater than the cathodic Tafel slope (β_c), indicating the coated sample's tendency toward passivation in the corrosive environment [51]. A comparison of the polarization curves reveals that the coating predominantly influences the anodic reaction kinetics compared to the cathodic process, signifying that the anodic dissolution of the substrate is more strongly inhibited than the hydrogen evolution reaction. This behavior leads to a transition of E_{corr} toward more noble values, suggesting a decrease in the thermodynamic drive for corrosion. Since the shift toward more noble potentials is predominantly governed by the polarization of the anodic reactions, the coating demonstrates an anodic inhibition mechanism that effectively suppresses the dissolution rate of the steel substrate [52,53].

It is worth noting that the corrosion potentials of the coated samples fall within the passive potential region of the bare steel, which significantly mitigates the risk of localized corrosion initiation on the coated surfaces [54]. Moreover, in both simulated media, the coated sample demonstrates a lower corrosion current density, compared to the uncoated one, indicating that the cobalt coating significantly inhibits anodic dissolution of the steel substrate due to its superior chemical stability in the corrosive electrolyte [55]. The corrosion current density of the coated bipolar plate in both cathodic and anodic environment closely approaches the 2025 technology targets stipulated by the U.S. Department of Energy (DOE) for PEMFC applications.

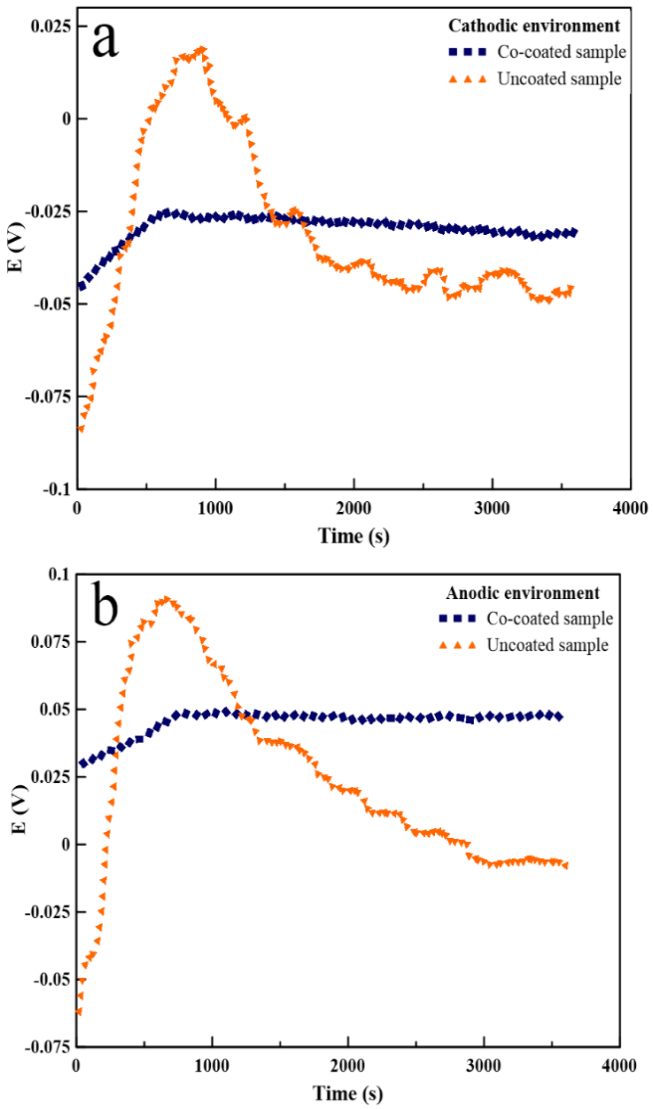

Fig. 6. Variation of corrosion potential with time for uncoated and Co-coated Crofer 22 APU steel in 0.5 M H_2SO_4 + 2 ppm HF solution at 70 °C in (a) cathodic and (b) anodic environments.

A comparison of the corrosion current densities of the steel bipolar plates coated in this study (1.79 μA cm^{-2}) with previously reported transition metal coatings for PEMFC applications [56-61] demonstrates that the current coating effectively enhances the corrosion resistance of the bipolar plates. Nevertheless, it is suggested that incorporating alternative transition metals alongside cobalt, or employing multi-layered cobalt-based coatings, could potentially yield even greater improvements in corrosion resistance.

3.2.3. Potentiostatic Polarization

The long-term electrochemical performance of the coatings in fuel cell cathodic and anodic environments was further evaluated through potentiostatic polarization tests. In these tests, the current density was continuously recorded as a function of time over a 2-hour period (Figure 8).

The current-time responses for both samples in the cathodic and anodic electrolytes initially showed a sharp decrease, followed by stabilization at nearly constant values. Notably, the coated sample exhibited smaller current fluctuations in the steady-state region compared with the uncoated sample. The steady-state current densities were approximately 63 and 26 μA cm^{-2} in the cathodic environment, and 36 and 19 μA cm^{-2} in the anodic environment for the uncoated and coated samples, respectively. The obtained results verify the protective role of the cobalt layer in limiting corrosive attack on the steel surface.

Table 2. Electrochemical data derived from potentiodynamic polarization curves of uncoated and coated samples.

Sample	Uncoated sample		Co-coated sample	
Environment	Cathodic	Anodic	Cathodic	Anodic
E_{corr} (mV)	-0.049 ±0.007	-0.003 ±0.001	-0.035 ±0.004	0.041 ±0.01
i_{corr} (μA cm^{-2})	56.3 ±2.1	36 ±1.8	1.79 ±0.05	1.43 ±0.02
β_c (mV dec^{-1})	-166 ±5.2	-155 ±3.5	-372 ±11.4	-519 ±6.7
β_a (mV dec^{-1})	773 ±3.1	1308 ±14.6	493 ±3.9	527 ±7.8
R_p (Ω cm^2)	1056 ±22.7	1675 ±8.8	51400 ±14.4	79500 ±20.6

3.2.4. Electrochemical Impedance Spectroscopy

The EIS results for the samples tested in simulated cathodic and anodic environments are illustrated in Figure 9. The impedance spectra were acquired over a frequency range of 0.01 Hz to 100 kHz. The equivalent electrical circuits employed for modeling the impedance data of the uncoated and coated specimens are presented in Figures 10a and 10b, respectively. In these circuits, Rs denotes the solution resistance between the reference electrode and the working electrode; Rct denotes the charge-transfer resistance of the steel substrate; Rcoat corresponds to the resistance of the coating to electrolyte penetration; and the constant phase element (CPE) accounts for non-ideal capacitive behavior.

The CPE is characterized by its admittance parameter (CPE-T) and power-law exponent (CPE-P). The CPE components associated with the coating and the substrate are designated as CPEdl and CPEcoat, respectively. The parameters extracted from curve fitting using ZView software are summarized in Table 3. The appearance of two distinct peaks in the Bode-phase plots of the coated sample indicates the presence of two electrochemical time constants.

The time constant at high frequencies reflects the behavior of the coating layer, while the low-frequency time constant arises from electrochemical processes at the coating–substrate interface [62].

The intersection point of the Nyquist curve with the real axis of the impedance plot (Z′) at high frequencies represents the solution resistance (R_s) [63].

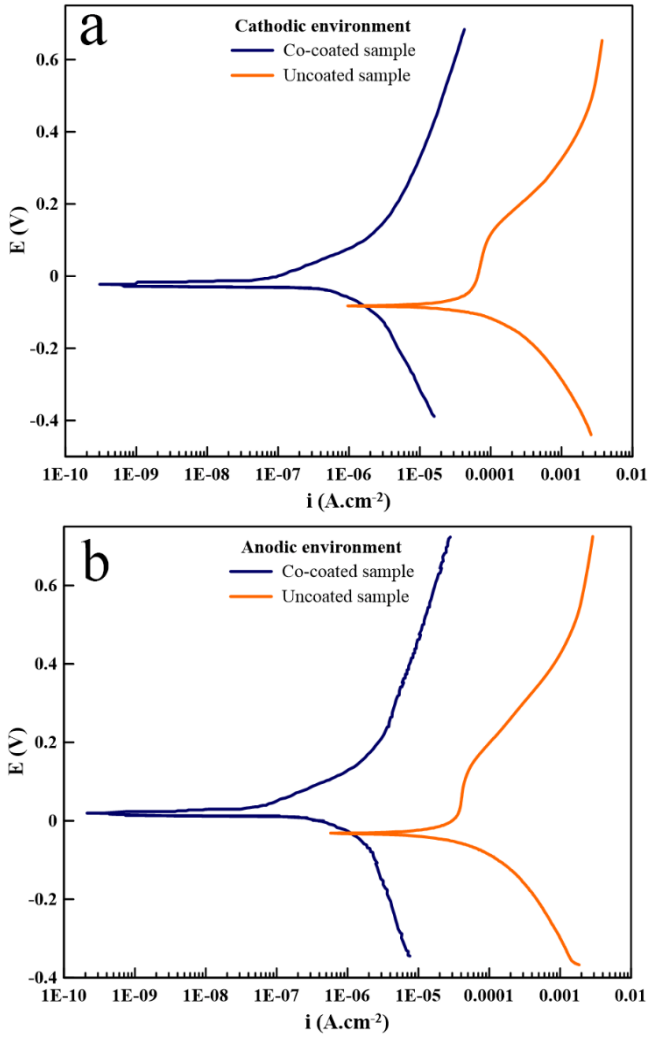

Fig. 7. Potentiodynamic polarization curves for uncoated and Co-coated Crofer 22 APU steel in 0.5 M H_2SO_4 + 2 ppm HF solution at 70 °C in (a) cathodic and (b) anodic environments.

The measured charge-transfer resistance (R_{ct}) for the uncoated and coated specimens were 6583 and 18300 Ω cm^2, respectively, in the anodic environment, and 6451 and 16920 Ω cm^2, respectively, in the cathodic environment. While R_{ct} characterizes the ion-transport resistance through the coating in coated specimens, it denotes the stability of the passive film in uncoated ones [64]. The significantly higher R_{ct} of the coated samples in both conditions demonstrates the beneficial effect of cobalt deposition in enhancing the corrosion resistance of the steel substrate.

Furthermore, the larger phase angle observed at high frequencies for the coated sample confirms its improved electrochemical stability [65]. The lower double-layer admittance values in both simulated environments also indicate that the surface passivation of the cobalt coating effectively impedes the penetration of aggressive ions toward the steel substrate. Sulfuric acid dissociates in an aqueous medium according to the following reactions [66]:

$$H_2SO_4 \rightarrow HSO_4^- + H^+ \quad (5)$$

$$HSO_4^- \rightarrow SO_4^{2-} + H^+ \quad (6)$$

The dissociation constant of reaction (5) is significantly higher than that of reaction (6). Consequently, in dilute and moderately concentrated solutions, sulfuric acid fully dissociates according to reaction (6), making the SO_4^{2-} ion the predominant corrosive species. In the presence of these ions, iron can dissolve into the solution as $FeSO_4$ [66].

Owing to the high chromium content in ferritic stainless steels, protective surface films composed of chromium oxide-hydroxide compounds are formed through the following reactions, leading to the surface passivation and enhanced corrosion resistance [67]:

$$Cr + H_2SO_4 \rightarrow CrOOH + SO_2 + H^+ + e^- \quad (7)$$

$$4Cr + 3H_2SO_4 \rightarrow 2Cr_2O_3 + 3SO_2 + 6H^+ + 6e^- \quad (8)$$

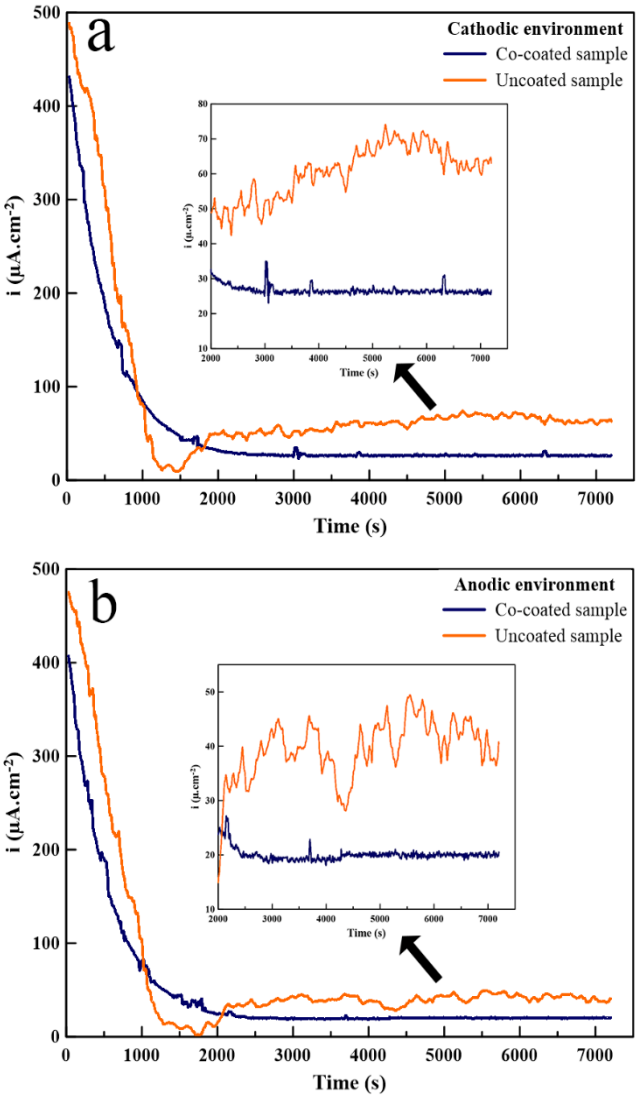

Fig. 8. Potentistatic polarization curves for uncoated and Co-coated Crofer 22 APU steel in 0.5 M H_2SO_4 + 2 ppm HF solution at 70 °C in (a) cathodic and (b) anodic environments.

However, as shown in the subsequent reactions, the dissolution of this protective layer can expose the metal substrate to the corrosive environment again [64]:

$$CrOOH + H_2SO_4 + H^+ + e^- \rightarrow CrSO_4 + 2H_2O \quad (9)$$

$$Cr_2O_3 + 2H_2SO_4 + 2H^+ + 2e^- \rightarrow 2CrSO_4 + 3H_2O \quad (10)$$

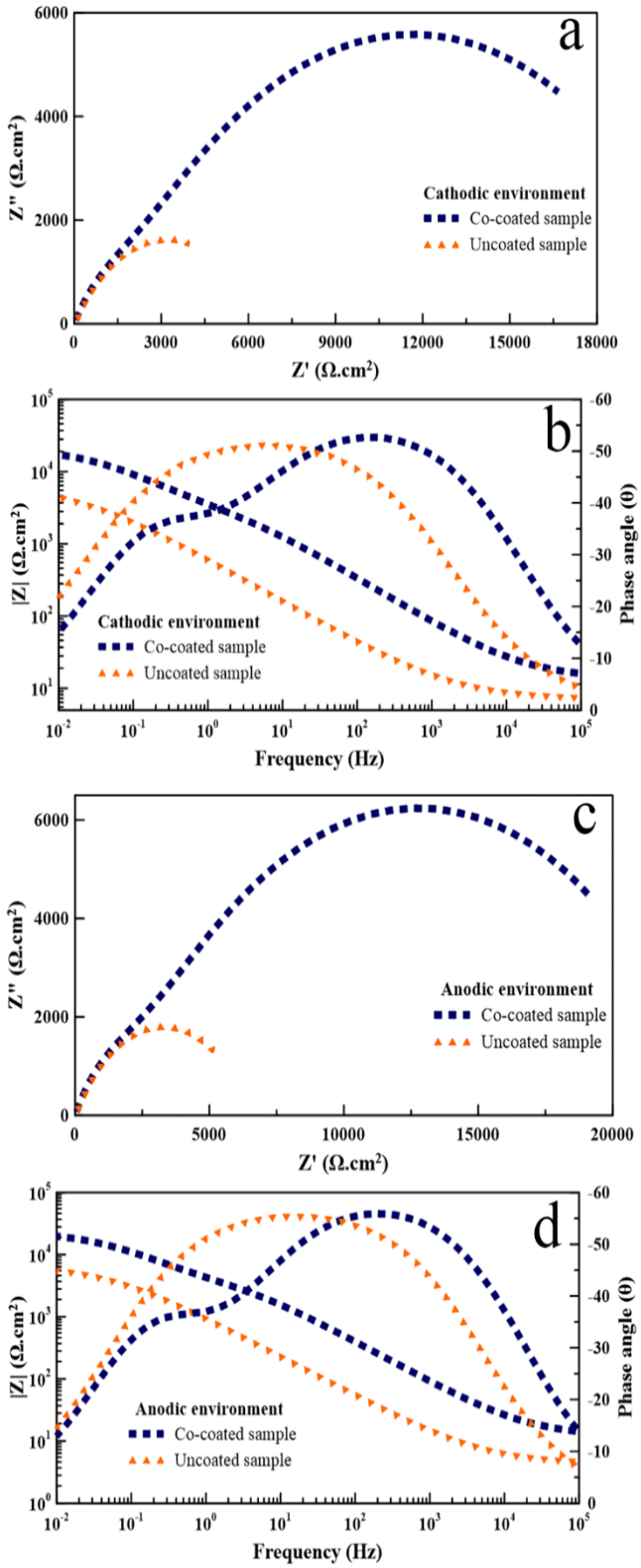

Fig. 9. Nyquist, Bode and Bode-phase curves for uncoated and Co-coated Crofer 22 APU steel in 0.5 M H_2SO_4 + 2 ppm HF solution at 70 °C in (a) cathodic and (b) anodic environments.

The application of surface coatings, particularly those based on transition metals such as cobalt, can further improve the corrosion resistance of steel. This improvement stems from the formation of a stable protective layer, typically consisting of oxides or hydrated oxides of the coating metal. When cobalt-coated steel is exposed to corrosive conditions, a film of CoO or $Co(OH)_2$ develops on the surface. If these layers dissolve in the corrosive medium, the steel substrate becomes susceptible to corrosion. In such cases, corrosion often initiates at high-energy sites within the coating structure, including grain boundaries and triple junctions [68,69].

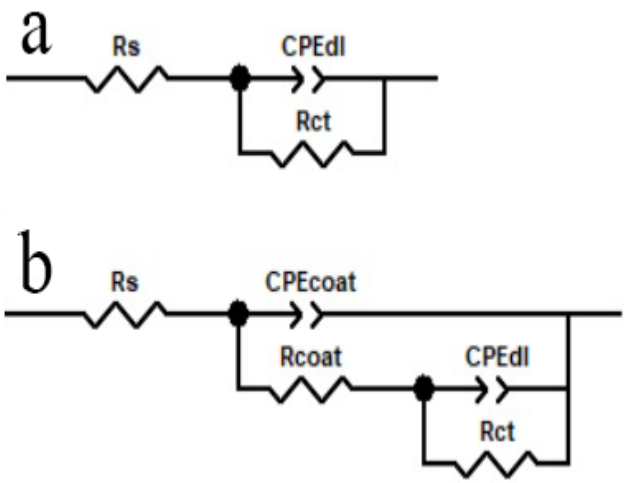

Fig. 10. The equivalent circuit used to adjust the EIS data of the (a) uncoated and (b) Co-coated Crofer 22 APU steel.

3.3. XPS Study

XPS analysis was performed to examine the chemical states of the sample surfaces following potentiostatic polarization in a cathodic medium for 2 hours. The high-resolution spectra for iron, chromium, sulfur, and oxygen (in the uncoated sample) are presented in Figure 11. The Fe 2p spectrum (Figure 11a) shows peaks at binding energies of 706.7, 708.9, 710, 710.9, 712, and 714.7 eV, attributed to FeO, Fe_3O_4, FeO or FeS, Fe_2O_3, $FeSO_4$, and $Fe_2(SO_4)_3$, respectively. These peaks in the XPS analysis of steel alloys after exposure to sulfuric acid environments have also been reported by other researchers [67, 69, 70]. These species have also been documented in previous XPS studies of steel alloys exposed to sulfuric acid media.

The Cr 2p spectrum (Figure 11b) exhibits four distinct peaks corresponding to metallic Cr (574 eV), Cr_2O_3 or CrOOH (576.5 eV), $Cr(OH)_3$ (577.4 eV), and $Cr_2(SO_4)_3$ (578.6 eV) [67, 69, 71]. The S 2p1/2 peaks at 163.1 and 169.8 eV, along with the S 2p3/2 peaks at 162 and 168.7 eV (Figure 11c), suggest S^{2-} and SO_4^{2-} species within the surface layer [67, 72].

In the O 1s spectrum (Figure 11d), peaks observed at 530.2, 531.4, and 532.6 eV match metal-oxygen (M-O) bonds, hydroxide ions (OH^-), and sulfate ions (SO_4^{2-}), respectively.

The hydroxide peak indicates the formation of $Cr(OH)_3$ phases within the passive layer, whereas the SO_4^{2-} peak evidences the incorporation of compounds such as $FeSO_4$ and $Cr_2(SO_4)_3$ into the protective film [69].

Fig. 12 presents the high-resolution XPS spectra of the coated surface after polarization. The binding energy separation of 15.8 eV between the Co 2p1/2 (795.9 eV) and Co 2p3/2 (780.1 eV) peaks in Figure 12a suggests the presence of CoO on the surface [73]. Additionally, the O 1s spectrum (Fig. 12b) displays three peaks at 530.2, 531.4, and 532.6 eV, corresponding to O^{2-} ions in CoO, OH^- groups, and adsorbed H_2O molecules, respectively [74].

Table 3. Electrochemical data derived from EIS curves of uncoated and coated samples.

Sample	Uncoated sample		Co-coated sample	
Environment	Cathodic	Anodic	Cathodic	Anodic
R_s (Ω cm^2)	6.78	4.14	13.4	11.9
R_{ct} (Ω cm^2)	6451	6583	16920	18300
CPE-$T_{dl}\times10^6$ (Ω^{-1} cm^{-2} S^n)	552	320	103	91.4
CPE-P_{dl} (Ω^{-1} cm^{-2} S^n)	0.596	0.639	0.656	0.682
R_{coat} (Ω cm^2)	-	-	4740	5123
CPE-$T_{coat}\times10^6$ (Ω^{-1} cm^{-2} S^n)	-	-	47.6	32.2
CPE-P_{coat} (Ω^{-1} cm^{-2} S^n)	-	-	0.64	0.673

3.4. Interfacial contact resistance (ICR)

Fig. 13 presents the variation in ICR of the tested samples before and after potentiodynamic polarization in both cathodic and anodic media. As applied pressure increases, the ICR values initially drop drastically and then gradually stabilize. This trend stems from the enlargement of the effective contact area between the sample and the GDL under higher pressures.

The enhanced contact area facilitates more uniform current distribution, thereby improving electrical conductivity [75]. According to the U.S. Department of Energy (DOE) specifications, the ICR of bipolar plates should remain below 10 mΩcm^2 at an applied pressure of 1.4 MPa. At this pressure, the uncoated and coated samples exhibited ICR values of 30.49 and 2.42 mΩcm^2, respectively, prior to polarization. After testing, these values increased to 45.68 and 3.87 mΩ cm^2 in the cathodic environment, and 38.45 and 3.25 mΩ cm^2 in the anodic environment.

The increase in ICR following polarization is a consequence of the nature and thickness of the passive films formed on the sample surfaces. Before polarization, passive layers form in ambient air, while during polarization, they develop in oxygen-rich conditions, producing thicker layers and consequently higher ICR values [30, 76]. The higher electrical resistance observed for the uncoated steel after corrosion results from the formation of insulating phases such as Cr_2O_3 and CrOOH within the passive layer. In contrast, the cobalt oxide film formed on the coated sample surface demonstrates superior electrical conductivity, accounting for its lower ICR values [77, 78].

The ICR values of the coating developed in this study, both before and after polarization, exhibited superior stability and lower magnitudes compared to many coatings reported in the literature. This enhanced performance can be attributed to the intrinsic metallic nature of the cobalt coating [79-84].

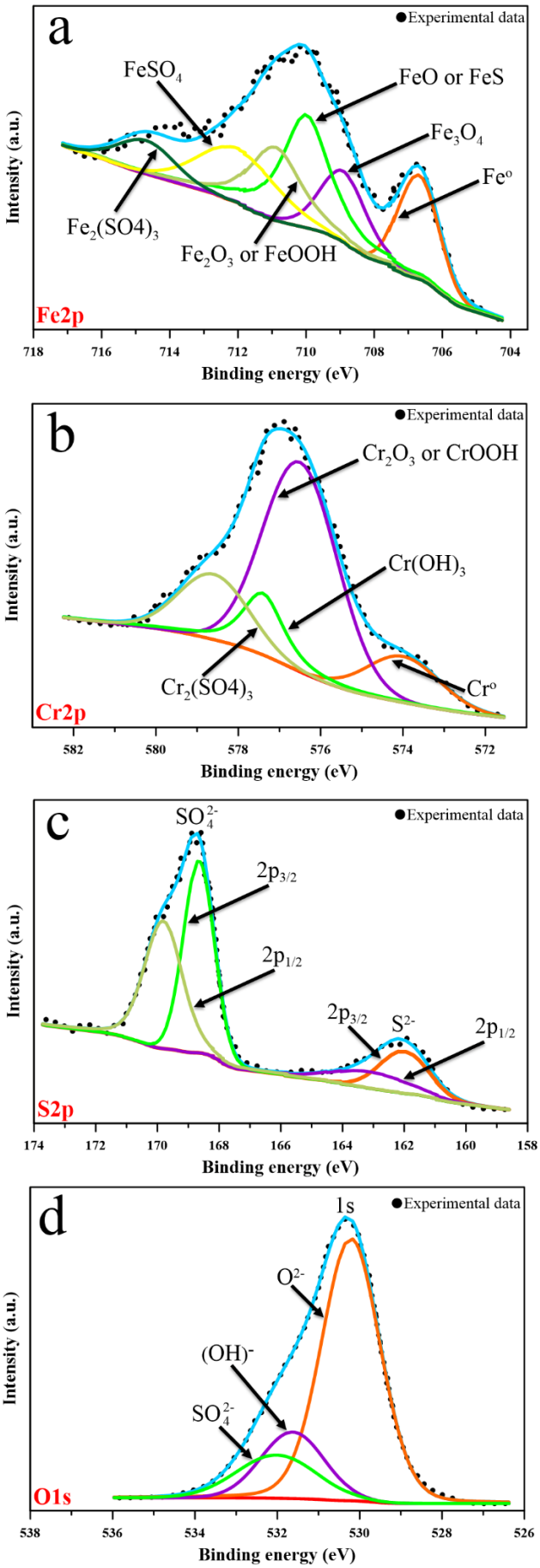

Fig. 11. High-resolution XPS results for uncoated Crofer 22 APU steel after potentiostatic polarization in 0.5 M H_2SO_4 + 2 ppm HF at 70 °C in cathodic environments for (a) Fe2p spectra, (b) Cr2p spectra, (c) S2p spectra, and (d) O1s spectra.

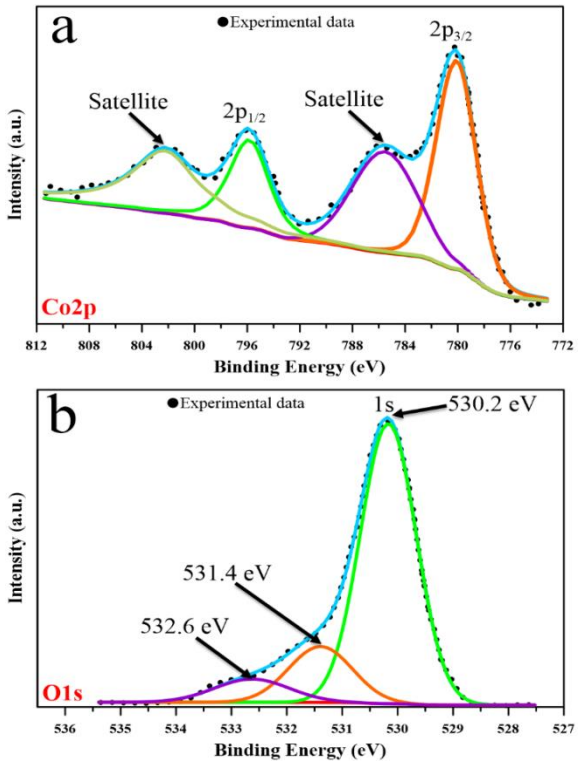

Fig. 12. High-resolution XPS results for Co-coated Crofer 22 APU steel after potentiostatic polarization in 0.5 M H_2SO_4 + 2 ppm HF at 70 °C in cathodic environments for (a) Co2p spectra and (b) O1s spectra.

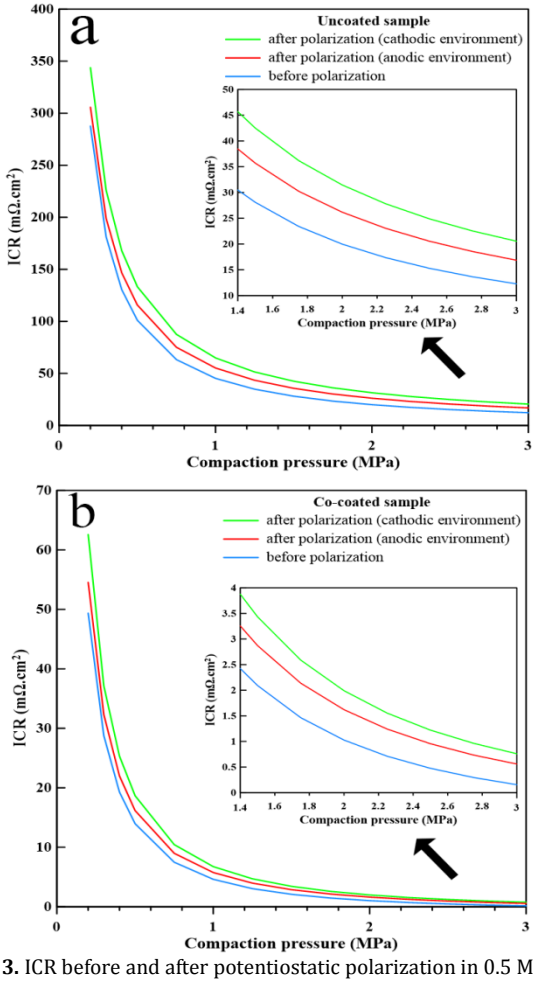

Fig. 13. ICR before and after potentiostatic polarization in 0.5 M H_2SO_4 + 2 ppm HF at 70 °C in cathodic and anodic environments for the (a) uncoated and (b) Co-coated steel.

Although controlled laboratory experiments offer a high degree of precision, they remain constrained in their ability to fully replicate real-world operating conditions. In practical applications, abrupt variations in temperature and humidity, the presence of environmental contaminants, non-uniform water and gas distribution, and stresses arising from repeated start-stop cycles may collectively give rise to discrepancies between laboratory-scale results and actual fuel cell performance. Therefore, long-term durability testing is strongly recommended to provide a more robust and reliable assessment of fuel cell behavior under realistic operating conditions. Moreover, for a more comprehensive evaluation of bipolar plate performance, detailed investigation of surface hydrophobicity and surface topography should also be taken into consideration.

4. Conclusions

A metallic cobalt coating, characterized by a cauliflower-like morphology and a thickness of 15 µm, was successfully electrodeposited on a Crofer 22 APU stainless steel substrate. Experimental results indicate that the coated samples exhibited corrosion potentials overlapping with the passive region of the bare substrate. This phenomenon enabled the coating to serve as an efficient barrier against the corrosive environment, resulting in a significant reduction in the measured current density. Furthermore, post-polarization XPS analysis revealed that the formation of cobalt oxide contributed to the enhanced corrosion resistance of the coated sample. The cobalt coating significantly improved the electrical performance of the steel substrate by inhibiting the formation of low-conductivity passive films, which typically emerge on the bare steel during polarization and lead to elevated ICR values.

Funding Statement

This research received no specific grant from any funding agency.

Conflicts of Interest

The authors declare no conflicts of interest.

Authors Contribution Statement

All authors contributed equally to this work.

References

[1] Sharma, P., and Pandey, O.P., Proton exchange membrane fuel cells: fundamentals, advanced technologies, and practical applications, in: Kaur, G., (Eds.), PEM Fuel Cells, Elsevier, Amsterdam, 2022, pp. 1-24.

[2] Qasem, N.A.A., and Abdulrahman, G.A.Q., 2024. A recent comprehensive review of fuel cells: history, types, and applications. *International Journal of Energy Research*, 2024, pp.7271748-7271783.

[3] Tawalbeh, M., Alarab, S., Al-Othman, A., and Javed, R.M.N., 2022. The operating parameters, structural composition, and fuel sustainability aspects of PEM fuel fells: a mini review. *Fuels*, 3, pp.449-474.

[4] Majlan, E.H., Rohendi, D., Daud, W.R.W., Husaini, T. and Haque, M.A., 2018. Electrode for proton exchange membrane fuel cells: A review. *Renewable and Sustainable Energy*, 89, pp.117-134.

[5] Rafiq, A., Rishikesh, K., Vignarooban, K., and Kannan, A.M., 2024. Optimized anode, cathode, and coolant flow designs for enhanced performance of proton exchange membrane fuel cells. *International Journal of Hydrogen Energy*, 50, pp.1302-1313.

[6] Mandal, P., kumar Chanda, U. and Roy, S., 2018. A review of corrosion resistance method on stainless steel bipolar plate. *Materials Today: Proceedings,* 5(9), pp.17852-17856.

[7] Thompson, S.T., James, B.D., Huya-Kouadio, J.M., DeSantis, D.A., Ahluwalia, R., Wilson, A.R., Kleen, G. and Papageorgopoulos, D., 2018. Direct hydrogen fuel cell electric vehicle cost analysis: system and high-volume manufacturing description, validation, and outlook. *Journal Power Sources*, 399, pp.304-313.

[8] Zhang, C., Ma, J., Liang, X., Luo, F., Cheng, R. and Gong, F., 2018. Fabrication of metallic bipolar plate for proton exchange membrane fuel cells by using polymer powder medium based flexible forming. *Journal of Materials Processing Technology*, 262, pp.32-40.

[9] Wang, J., Wang, H. and Fan, Y., 2018. Techno-economic challenges of fuel cell commercialization. *Engineering*, 4(3), pp.352-360.

[10] Silva, R.F., Franchi, D., Leone, A., Pilloni, L., Masci, A. and Pozio, A., 2006. Surface conductivity and stability of metallic bipolar plate materials for polymer electrolyte fuel cells. *Electrochimica Acta*, 51(17), pp.3592-3598.

[11] Wilberforce, T., Ijaodola, O., Baroutaji, A., Ogungbemi, E. and Olabi, A.G., 2022. Effect of bipolar plate material on proton exchange membrane fuel cell performance. *Energies*, 15(5), pp.1886-1900.

[12] Wang, H., and Turner, J.A., 2010. Reviewing metallic PEMFC bipolar plates. *Fuel Cell*, 10(4), pp.510-519.

[13] Cunningham, B.D., Huang, J., and Baird, D.G., 2007, Review of materials and processing methods used in the production of bipolar plates for fuel cells. *International Materials Reviews*, 52(1), pp.1-13.

[14] Gao, X., Chen, J., Xu, R., Zhen, Z., Zeng, X., Chen, X. and Cui, L., 2024. Research progress and prospect of the materials of bipolar plates for proton exchange membrane fuel cells (PEMFCs). *International Journal of Hydrogen Energy*, 50, pp.711-743.

[15] Yuxi, S., Caizhi, Z., Chun-Yu, L., Ming, H., Rui-Yuan, Y., Deen, S. and Jinrui, C., 2020. Review on current research of materials, fabrication, and application for bipolar plate in proton exchange membrane fuel cell. *International Journal of Hydrogen Energy*, 45(54), pp.29832-29847.

[16] Mousavi Ehteshami, S.M., Taheri, A., and Chan, S.H., 2016. A review on ions induced contamination of polymer electrolyte membrane fuel cells, poisoning mechanisms, and mitigation approaches. *Journal of Industrial and Engineering Chemistry*, 34, pp.1-8.

[17] Karimi, S., Fraser, N., Roberts, B., and Foulkes, F.R., 2012. A review of metallic bipolar plates for proton exchange membrane fuel cells: Materials and fabrication methods. *Advances in Materials Science and Engineering*, 2012, pp.1-22.

[18] Papadias, D.D., Ahluwalia, R.K., Thomson, J.K., Meyer, H.M., Brady, M.P., Wang, H., Turner, J.A., Mukundan, R. and Borup, R., 2015. Degradation of SS316L bipolar plates in simulated fuel cell environment: Corrosion rate, barrier film formation kinetics and contact resistance. *Journal of Power Sources*, 273, pp.1237-1249.

[19] Andre, J., Antoni, L., Petit, J.-P., De Vito, E. and Montani, A., 2009. Electrical contact resistance between stainless steel bipolar plate and carbon felt in PEFC: A comprehensive study. *International Journal of Hydrogen Energy*, 34(7), pp.3125-3133.

[20] Wang, Y., Chen, K.S., Mishler, J., Cho, S.C. and Adroher, X.C., 2011. A review of polymer electrolyte membrane fuel cells: Technology, applications, and needs on fundamental research. *Applied Energy*, 88(4), pp.981-1007.

[21] Mehta, V., and Cooper, J.S., 2003. Review and analysis of PEM fuel cell design and manufacturing. *Journal of Power Sources*, 114(1), pp.32-53.

[22] Miyazawa, A., Tada, E., and Nishikata, A., 2013. Influence of corrosion of SS316L bipolar plate on PEFC performance. *Journal of Power Sources*, 231, pp.226-233.

[23] Yi, P., Zhang, D., Qiu, D., Peng, L., and Lai, X., 2019. Carbon-based coatings for metallic bipolar plates used in proton exchange membrane fuel cells. *International Journal of Hydrogen Energy*, 44(13), pp.6813-6843.

[24] Ijaodola, O., Ogungbemi, E., Khatib, F.N., Wilberforce, T., Ramadan, M., El Hassan, Z., Thompson, J. and Olabi, A.G., 2018. Evaluating the effect of metal bipolar plate coating on the performance of proton exchange membrane fuel cells. *Energies*, 11(11), pp.3203-3230.

[25] Hong, S.T., Scott, Weil, K., Bae, In.-Tae., Choi, J.P. and Pan, J., 2010. Annealing induced interfacial layers in niobium-clad stainless steel developed as a bipolar plate material for polymer electrolyte membrane fuel cell stacks. *Journal of Power Sources*, 195(9), pp.2592-2598.

[26] Chanda, U.K., Padhee, S.P., Pathak, A.D., Roy, S. and Pati, S., 2019. Effect of Cr content on the corrosion resistance of Ni-Cr-P coatings for PEMFC metallic bipolar plates. *Materials for Renewable and Sustainable Energy*, 8(4), p.20.

[27] Cao, C., Liang, C. and Huang, N., 2015. Electrochemical behavior of niobium electrodeposited 316 stainless steel bipolar plate for PEMFC in choline chloride based ionic liquids. *Journal of Wuhan University of Technology – Materials Science Edition*, 30(5), pp.1061-1067.

[28] Ingle, A.V., Raja, V.S., Rangarajan, J. and Mishra, P., 2020. Corrosion resistant quaternary Al-Cr-Mo-N coating on type 316L stainless steel bipolar plates for

proton exchange membrane fuel cells. *International Journal of Hydrogen Energy*, 45(4), pp.3094-3107.

[29] Cho, K.H., Lee, W.G., Lee, S.B. and Jang, H., 2008. Corrosion resistance of chromized 316L stainless steel for PEMFC bipolar plates. *Journal of Power Sources*, 178(2), pp.671-676.

[30] Feng, K., Shen, Y., Liu, D., Chu, P.K. and Cai, X., 2010. Ni-Cr Co-implanted 316L stainless steel as bipolar plate in polymer electrolyte membrane fuel cells. *International Journal of Hydrogen Energy*, 35(2), pp.690-700.

[31] Manso, A.P., Marzo, F.F., Garicano, X., Alegre, C., Lozano, A., and Barreras, F., 2020. Corrosion behavior of tantalum coatings on AISI 316L stainless steel substrate for bipolar plates of PEM fuel cells, *International Journal of Hydrogen Energy*, 45(40), pp.20679-20691.

[32] Atapour, M., Rajaei, V., Trasatti, S., Casaletto, M.P. and Chiarello, G.L., 2020. Thin niobium and niobium nitride PVD coatings on AISI 304 stainless steel as bipolar plates for PEMFCs. *Coatings*, 10(9), pp.889-905.

[33] Huang, I. and Hwang, C.C., 2015. Surface treatments of stainless steel by electroless silver coatings as a bipolar plate for proton exchange membrane fuel cells. *Journal of fuel Cell Science and Technology*, 12(6), pp.061001-061005.

[34] Chiang, T.-Y., A-S, Tsai, L.-C., Lee, H.-B., Lin, C.-Y., Sheu, H.-H. and Chang, C.-C., 2015. Effect of metal bipolar plate channel fabrication on electroplating - using nickel electroplating of AISI 1045 channel substrate as an example. *International Journal of Electrochemical Science*, *10*, pp.1926-1939.

[35] Rashtchi, H., Raeissi, K., Shamanian, M., Acevedo Gomez, Y., Lagergren, C., Wreland Lindström, R. and Rajaei, V., 2016. Evaluation of Ni-Mo and Ni-Mo-P electroplated coatings on stainless steel for PEM fuel cells bipolar plates. *Fuel Cells*, 16(6), pp.784-800.

[36] Li, T., Zhang, P.C., Liu, K., Xu, S., Han, Y.T., Shi, J.F., Sun, J.C., 2019. Performance of tantalum modified 316L stainless steel bipolar plate for proton exchange membrane. *Fuel Cell*, 19(6), pp.724-730.

[37] Cui, J., Yao, Z., Cheng, F., Cui, Y., Wang, G., Wang, L., Sun, H., Li, S., Wen, Z., and Sun, J., 2016. Corrosion resistance of a tungsten modified AISI 430 stainless steel bipolar plate for proton exchange membrane fuel cells. *RSC Advances*, 6(37), pp.31367-31373.

[38] Nikolov, K., Bunk, K., Jung, A., Gerlach, J.W., Kaestner, P., and Klages, C.P., 2017. Combined plasma surface modification of austenitic stainless steel for bipolar plates. *Surface and Coatings Technology*, 328, pp.142-151.

[39] Wang, L., Sun, J., Li, P., Jing, B., Li, S., Wen, Z., and Ji, S., 2012. Niobized AISI 304 stainless steel bipolar plate for proton exchange membrane fuel cell. *Journal of Power Sources*, 208, pp.397-403.

[40] Kang, H.E., Choi, J.H., Lee, U., Kim, H.G., and Yoon, Y.S., 2024. Characterization of CrAl coating on stainless steel bipolar plates for polymer electrolyte membrane fuel cells. *International Journal of Hydrogen Energy*, 51, pp.1208-1226.

[41] Kumar, A.M., Ehsan, M.A., Suleiman, R.K., Ramana Murthy, R.V.V., Anjum Ahmed, B. and Javid, M., 2024. Bimetallic CuNi alloy coatings on SS304 substrate for bipolar plates of proton exchange membrane fuel cells. *ACS Applied Energy Materials*, 7(11), pp.4879-4890.

[42] Johar, M., Moradizadeh, L., Gupta, A., Mehdizadeh Chellehbari, Y., Li, X., and Shahgaldi, S., 2025. Development of novel Nb and Ta multilayer coatings for corrosion protection of Ti-based bipolar plates for proton exchange membrane fuel cells. *Corrosion Science*, 245, p.112707.

[43] Gago, A.S., Sanchez, D.G., Ansara, A.S., Gazdzicki, P., Wagner, N., Arnold, J., and Friedrich, K.A., 2015. Improved water management with thermally sprayed coatings on stainless steel bipolar plates of PEMFC. *ECS Transactions*, 69(17), pp.223-240.

[44] Aledresse, A., and Alfantazi, A., 2004. A study on the corrosion behavior of nanostructured electrodeposited cobalt. *Journal of Materials Science*, 39(4), pp.1523–1526.

[45] Wang, H., Turner, J.A., Li, X. and Bhattacharya, R., 2007. SnO_2:F coated austenite stainless steels for PEM fuel cell bipolar plates. *Journal of Power Sources*, 171(2), pp.567-574.

[46] Nakahara, S., and Mahajan, S., 1980. The Influence of Solution pH on Microstructure of Electrodeposited Cobalt. *Journal of The Electrochemical Society*, 127(2), pp.283-287.

[47] Kerrigan, M.M., Klesko, J.P. and Winter, C.H., 2017. Low Temperature, Selective Atomic Layer Deposition of Cobalt Metal Films Using Bis(1,4-di-tert-butyl-1,3-diazadienyl) cobalt and Alkylamine Precursors. *Chemistry of Materials*, 29(17), pp.7458-7466.

[48] Li, G., Zhang, L., Cai, F., Yang, Y., Wang, Q. and Zhang, S., 2019. Characterization and corrosion behaviors of TiN/TiAlN multilayer coatings by ion source enhanced hybrid arc ion plating. *Surface and Coating Technology*, 366, pp.355-365.

[49] Kwak, J., Jung, S.M., Kim, K.S., Choe, G., Son, S., Kim, H.S., and Kim, Y.T., 2025. Fe–N–C surface treatment as method for enhancing spontaneous passivation of low Ni and Cr stainless steel. *Applied Surface Science Advances*, 30, p.100871.

[50] Reclaru, L. and Ardelean, L.C., 2020. Corrosion Susceptibility and Allergy Potential of Austenitic Stainless Steels. *Materials*, 13(18), pp.4187-4210.

[51] Fetohi, A.E., Abdel Hameed, R.M., El-Khatib, K.M., and Souaya, E.R., 2012. Ni-P and Ni-Co-P coated aluminum alloy 5251 substrates as metallic bipolar plates for PEM fuel cell applications. *Journal of Hydrogen Energy*, 37(9), pp.7677-7688.

[52] Wang, X.Z. Luo, H., Muneshwar, T., Fan, H.Q., Cadien, K., and Luo, J.L., 2018. Zr_2N_2O Coating-Improved Corrosion Resistance for the Anodic Dissolution Induced by Cathodic Transient Potential. *ACS Applied Materials & Interfaces*, 10(46), pp.40111-40124.

[53] Peng, J., Ji, G., Shi, Z., and Wang, X., 2021. Numerical Simulation Based on a ZrO_2-Coated Stainless-Steel Corrosion Experiment. *ACS Omega*, 6(22), pp.14507-14517.

[54] Gamboa, S.A., Gonzalez-Rodriguez, J.G., Valenzuela, E., Campillo, B., Sebastian, P.J., and Reyes-Rojas, A., 2006. Evaluation of the corrosion resistance of Ni-Co-B coatings in simulated PEMFC environment. *Electrochimical Acta*, 51(19), pp.4045-4051.

[55] Wang, L., Sun, J.C., and Xu, X.L., 2001. Low pressure plasma arc source ion nitriding compared with glow-discharge plasma nitriding of stainless steel. *Surface and Coating Technology*, 145(1-3), pp.31-37.

[56] St, einhorst, M., Auinger, M., Roch, T., and Leyens, C., 2023. Modelling and corrosion of coated stainless steel substrates for bipolar plates at different temperatures. *Journal of Applied Electrochemistry*, 53(7), pp.1491–1503.

[57] Jin, X., Zhu, R., Zhu, Y., and Li, M., 2025. Preparation and electrochemical corrosion of Cr–C coatings by cathode plasma electrolytic deposition for stainless steel bipolar plate in PEMFC. *Journal of Materials Research and Technology*, 37, pp.1669-1681.

[58] Avram, D.N., Davidescu, C.M., Hulka, I., Dan, M.L., Stanciu, E.M., Pascu, A., and Mirza-Rosca, J.C., 2023. Corrosion Behavior of Coated Low Carbon Steel in a Simulated PEMFC Environment. *Materials*, 16(8), pp.3056-3070.

[59] Dong, Z., Zhou, T., Liu, J., Zhang, X., Shen, B., Hu, W., and Liu, L., 2019. Performance of surface chromizing layer on 316L stainless steel for proton exchange membrane fuel cell bipolar plates. *International Journal of Hydrogen Energy*, 44(39), pp.22110-22121.

[60] Wang, L., Li, L., Liu, H., Wang, S., Fang, H., Gao, H., Gao, K., Zhang, Y., Sun, J., and Yan, J., 2018. Polylaminate TaN/Ta coating modified ferritic stainless steel bipolar plate for high temperature proton exchange membrane fuel cell. *Journal of Power Sources*, 399, pp.343-349.

[61] Rajaei, V., Rashtchi, H., Raeissi, K., and Shamanian, M., 2017. The study of Ni-based nano-crystalline and amorphous alloy coatings on AISI 304 stainless steel for PEM fuel cell bipolar plate application. *International Journal of Hydrogen Energy*, 42(20), pp.14264-14278.

[62] Alishahi, M., Mahboubi, F., Mousavi Khoie, S.M., Aparicio, M., Lopez-Elvira, E., Méndez, J. and Gago, R., 2016. Structural properties and corrosion resistance of tantalum nitride coatings produced by reactive DC magnetron sputtering. *RSC Advances*, 6(92), pp.89061-89072.

[63] Salehi, S., Aghazadeh, M., and Karimzadeh, I., 2022. Zn-MOF electrode material for supercapacitor applications, *Progress in Physics of Applied Materials*, 2(1), pp.77-81.

[64] Li, X., Sun, W., Zheng, Y., Long, C., and Wang, Q., 2023. New Strategy for the Design of Anti-Corrosion Coatings in Bipolar Plates Based on Hybrid Organic–Inorganic Layers. *Molecules*, 28(7), pp.3279-3290.

[65] Yang, J., Li, J., Wu, Z., Xia, D.H., Zhang, Y., Li, Q., Qin, Z., and Hu, W., 2026. Sputtering power-dependent microstructure and corrosion behavior of Ti-doped TiC/α-C coatings for PEMFC bipolar plates. *Surface and Coatings Technology*, 525, p.133321.

[66] Sippola, H. and Taskinen, P., 2014. Thermodynamic properties of aqueous sulfuric acid. *Journal of Chemical and Engineering Data*, 59(8), pp.2389-2407.

[67] Kish, J.R., Ives, M.B. and Rodda, J.R., 2003. Anodic behaviour of stainless steel S43000 in concentrated solutions of sulphuric acid. *Corrosion Science*, 45(7), pp.1571-1594.

[68] Gong, J. and Zangari, G., 2006. Electrodeposition of copper-manganese alloy coatings for sacrificial corrosion protection. *ECS Transactions*, 1(13), pp.97-106.

[69] Yue, Y., Liu, C., Shi, P. and Jiang. M., 2018. Passivity of stainless steel in sulphuric acid under chemical oxidation. *Corrosion Engineering, Science and Technology*, 53(3), pp.173-182.

[70] Lai, W.Y., Zhao, W.Z., Yin, Z.F. and Zhang, J., 2012. EIS and XPS studies on passive film of AISI 304 stainless steel in dilute sulfuric acid solution. *Surface and interface analysis*, 44(4), pp.418-425.

[71] Keller, P. and Strehblow, H.-H., 2004. XPS investigations of electrochemically formed passive layers on Fe/Cr-alloys in 0.5 M H_2SO_4. *Corrosion Science*, 46(8), pp.1939-1952.

[72] Natarajan, R., Palaniswamy, N., Natesan, M. and Muralidharan, V.S., 2009. XPS analysis of passive film on stainless steel. *The Open Corrosion Journal*, 2(1), pp.114-124.

[73] Dedryvere, R., Laruelle, S., Grugeon, S., Poizot, P., Gonbeau, D. and Tarascon, J.-M., 2004. Contribution of X-ray photoelectron spectroscopy to the study of the electrochemical reactivity of CoO toward lithium. *Chemistry of Materials*, 16(6), pp.1056-1061.

[74] García-Gómez, A., Eugénio, S., Duarte, R.G., Silva, T.M., Carmezim, M.J., and Montemor, M.F., 2016. Electrodeposited reduced-graphene oxide/cobalt oxide electrodes for charge storage applications. *Applied Surface Science*, 382, pp.34-40.

[75] Selamet, O.F. and Ergoktas, M.S., 2015. Effects of bolt torque and contact resistance on the performance of the polymer electrolyte membrane electrolyzers. *Journal of Power Sources*, 281, pp.103-113.

[76] Rajasekar, S., Chetty, R. and Neelakantan, L., 2015. Low-nickel austenitic stainless steel as an alternative to 316L bipolar plate for proton exchange membrane fuel cells. *Journal of Hydrogen Energy*, 40(36), pp.12413-12423.

[77] Lee, J.B. and Oh, I.H., 2014. Electrochemical characteristics and interfacial contact resistance of multi-layered Ti/TiN coating for metallic bipolar-plate of polymer electrolyte membrane fuel cells. *Metals and Materials Internartional*, 20(4), pp.629-639.

[78] Lange, F. and Martin, M., 1997. The electrical conductivity of CoO: Experimental results and a new conductivity model. *Berichte der Bunsengesellschaft für physikalische Chemie*, 101(2), pp.176-184.

[79] Ding, G., Wang, C., Gao, N., Li, R., Wang, Y., and Ma, H., 2023. Superior conductive polypyrrole anti-corrosion coating doped with titanium nitride for 304 stainless steel bipolar plates. *Journal of Applied Polymer Science*, 140(12), p.e53639.

[80] Zhang, K., and Sharma, S., 2017. Site-Selective, Low-Loading, Au Nanoparticle–Polyaniline Hybrid Coatings with Enhanced Corrosion Resistance and Conductivity for Fuel Cells. *ACS Sustainable Chemistry & Engineering*, 5(1), pp.277-286.

[81] Ma, G., Yuan, J., Chen, R., Li, H., Wu, H., Yan, J., Wang, Z., and Wang, A., 2022. Balancing the corrosion resistance and conductivity of Cr-Al-C coatings via annealing treatment for metal bipolar plates. *Applied Surface Science*, 597, p.153670.

[82] Lu, J.L., Abbas, N., Tang, J.N., Tang, J., and Zhu, G.M., 2019. Synthesis and characterization of conductive ceramic MAX-phase coatings for metal bipolar plates in simulated PEMFC environments. *Corrosion Science*, 158, p.108106.

[83] Jin, J., Zhang, J., Hu, M., and Li, X., 2021. Investigation of high potential corrosion protection with titanium carbonitride coating on 316L stainless steel bipolar plates. *Corrosion Science*, 191, p.109757.

[84] Wang, H.C., Sheu, H.H., Lu, C.E., Hou, K.H., and Ger, M.D., 2015. Preparation of corrosion-resistant and conductive trivalent Cr–C coatings on 304 stainless steel for use as bipolar plates in proton exchange membrane fuel cells by electrodeposition. *Journal of Power Sources*, 293, pp.475-483.